PNAS RESEARCH ARTICLE | BIOCHEMISTRY OPEN ACCESS

Reverse-QTY code design of active human serum albumin self-assembled amphiphilic nanoparticles for effective anti-tumor drug doxorubicin release in mice

Run Meng[a], Shilei Hao[a,1], Changfa Sun[a], Zongkun Hou[a], Yao Hou[a], Lili Wang[a], Peiying Deng[a], Jia Deng[b], Yaying Yang[c], Haijian Xia[d], Bochu Wang[a,1], Rui Qing[e,1], and Shuguang Zhang[f,1]

Edited by William DeGrado, University of California San Francisco, San Francisco, CA; received November 26, 2022; accepted April 11, 2023

Human serum albumin (HSA) is a highly water-soluble protein with 67% alpha-helix content and three distinct domains (I, II, and III). HSA offers a great promise in drug delivery with enhanced permeability and retention effect. But it is hindered by protein denaturation during drug entrapment or conjugation that result in distinct cellular transport pathways and reduction of biological activities. Here we report using a protein design approach named reverse-QTY (rQTY) code to convert specific hydrophilic alpha-helices to hydrophobic to alpha-helices. The designed HSA undergo self-assembly of well-ordered nanoparticles with highly biological actives. The hydrophilic amino acids, asparagine (N), glutamine (Q), threonine (T), and tyrosine (Y) in the helical B-subdomains of HSA were systematically replaced by hydrophobic leucine (L), valine (V), and phenylalanine (F). HSA^{rQTY} nanoparticles exhibited efficient cellular internalization through the cell membrane albumin binding protein GP60, or SPARC (secreted protein, acidic and rich in cysteine)-mediated pathways. The designed HSA^{rQTY} variants displayed superior biological activities including: i) encapsulation of drug doxorubicin, ii) receptor-mediated cellular transport, iii) tumor cell targeting, and iv) antitumor efficiency compare to denatured HSA nanoparticles. HSA^{rQTY} nanoparticles provided superior tumor targeting and antitumor therapeutic effects compared to the albumin nanoparticles fabricated by antisolvent precipitation method. We believe that the rQTY code is a robust platform for specific hydrophobic modification of functional hydrophilic proteins with clear-defined binding interfaces.

alpha-helix engineering | hydrophilic to hydrophobic conversion | protein design | receptor-mediated drug delivery | treatment of mouse tumors

Significance

QTY code has been successfully used to significantly improve the solubility of water-insoluble integral transmembrane proteins. They include G protein-coupled receptors, cytokine receptors, glucose transporters, and solute carrier transporters through systematically replacing the hydrophobic leucine (L), valine (V), isoleucine (I), and phenylalanine (F) in the transmembrane domains by glutamine (Q), threonine (T), and tyrosine (Y). Here we reverse the QTY code as the reverse-QTY (rQTY) code to improve the hydrophobicity of the specific alpha-helices on human serum albumin for self-assembly into well-defined nanoparticles. The rQTY code has significant implications for design of specific hydrophobic domain of highly water-soluble proteins to design their self-assembly for diverse applications including encapsulate hydrophobic drugs, receptor-mediated sustained drug release and target the drug transport across cell membrane.

Human serum albumin (HSA) is the most abundant protein in plasma (~40 mg/L in blood) and a promising carrier for drug delivery since it is nontoxic, non-immunogenic, biocompatible and biodegradable (1–3). HSA preferential accumulation in solid tumors has inspired the development of rationally designed albumin nanoparticles for tumor targeting (4–7). Enhanced permeability and retention (EPR) effect can facilitate the accumulation and penetration of albumin-based nanoparticles in solid tumors (8, 9), whereas receptor-mediated active targeting represents another promising strategy for targeted specific drug delivery (10). For instance, albumin binds the 60 kDa glycoprotein (GP60, also known as albondin) receptor in endothelial cells and induces caveolin-dependent transcytosis, which contributes to albumin transcytosis across the tumor vasculature (11). SPARC (secreted protein acidic and rich in cysteine) is another critical albumin-binding protein that overexpresses in tumors and facilitates the efficacy of albumin nanoparticles uptake by tumor cells (12–14).

The past decade has witnessed significant advances in albumin-based drug delivery systems (15, 16). Nanoparticle albumin-bound (nab)-paclitaxel (PTX) named Abraxane was approved by the US Food and Drug Administration in 2005 for advanced cancer treatments (17). Several chemotherapeutic agents such as doxorubicin (DOX), cisplatin, methotrexate, and docetaxel have also been delivered using albumin nanoparticles for antitumor therapy in pre-clinical studies (10). However, traditional preparation processes for albumin-based nanoparticle complex require organic solvents, while albumin is prone to be denatured in such environments that may significantly reduce drug uptake by cells (18–20), and targeting tumor cell is an attractive approach for therapeutic intervention (21–24).

In order to avoid organic solvents, many attempts have been made to develop organic-solvent-free methods for the synthesis of albumin nanoparticles. PTX liposome-albumin composite nanoparticles were designed to avoid the direct contact of albumin with toxic organic solvents and enhance the colloidal stability of the formulation (19). PTX-PEG-HSA complex was also developed by dispersing PTX into PEG scaffold without using organic

This article is a PNAS Direct Submission.

[1]To whom correspondence may be addressed. Email: shilei_hao@cqu.edu.cn, wangbc2000@126.com, ruiqing.br@sjtu.edu.cn, or shuguang@mit.edu.

This article contains supporting information online at https://www.pnas.org/lookup/suppl/doi:10.1073/pnas.2220173120/-/DCSupplemental.

Published May 15, 2023.

solvents or Cremophor EL as solubilizers and then formulated with HSA into nanosuspensions suitable for intravenous administration (25). Furthermore, the bovine serum albumin (BSA) nanogel was synthesized through reaction between amino groups and polymers in phosphate buffer at room temperature without any organic molecules (26), while ionic liquid-based method was also used as an alternative technique (27).

Fabricating the albumin nanoparticles through self-assembly–based methods have also attracted considerable interests, which are relatively mild fabrication methods and driven by the hydrophobic interaction and/or hydrogen bonding in water compared to the de-solvation and emulsification approaches (10, 28–30). However, the self-assembly capability of native HSA is rather weak because of its homogeneous surface hydrophilicity.

Here we report a pathway using the reverse QTY code to design an amphiphilic HSA protein for nanoparticle fabrication through molecular self-assembly. The variant protein HSA^{rQTY} can effectively load with several kinds of chemotherapeutic agents. The method is called the reverse-QTY (rQTY) code. It is based on the original QTY code firstly reported on G protein-coupled receptors (GPCRs) in 2018 (31, 32). We later further expanded the QTY code to other integral membrane proteins including cytokine receptors.

QTY code is a simple tool for designs of water-soluble membrane proteins based on the similarity of chemical structures and electron density maps between polar and nonpolar amino acids, without extensive computational calculations. Pairwise amino acid substitutions were conducted where hydrophobic leucine (L), isoleucine (I)/valine (V), and phenylalanine (F) can be systematically substituted by hydrophilic glutamine (Q)/asparagine(N), threonine (T), and tyrosine (Y), respectively.

We asked if the QTY code can be reversed as the rQTY code, namely, to covert hydrophilic alpha-helix into hydrophobic alpha-helix since the code is simple and the change is pairwise. Therefore, the rQTY variants could become partially hydrophobic proteins at specific sites. If the rQTY code can replace amino acids Q, T, Y to L, V and F, respectively, it can then increase the hydrophobicity of the specific alpha-helices of HSA for efficient self-assembly into well-defined nanoparticles. In this study, we conclusively demonstrated that the reverse QTY code can indeed be applied to design HSA that undergo self-assembly in aqueous solution to form nanoparticles with defined critical micelle concentration (CMC) and size distributions, while the native HSA cannot.

Biological activities of these HSA^{rQTY} nanoparticles were found superior to those prepared by commonly used de-solvation method. We initially designed and synthesized three HSA^{rQTY} variants in this study, and fabricated DOX-loaded HSA^{rQTY} nanoparticles through self-assembly. HSA^{rQTY} nanoparticles were then evaluated as tumor-targeted drug carriers, which exhibited remarkably improved DOX delivery to the tumor microenvironment via albumin-binding proteins GP60 and SPARC. We show here that the HSA^{rQTY} variant nanoparticles can be used to effectively treat tumors in mice. Our experimental evidence demonstrated HSA^{rQTY} nanoparticles not only could effectively uptake into tumor cells, but they also significantly reduce tumor size and weight as well extend mice life span. Thus, it is possible this rQTY code could also be applied for other water-soluble proteins for various applications.

Results

Rational Design of Self-Assembling HSA using rQTY Code. HSA is a 585 amino acid protein with a molecular weight (MW) of 66.5 kDa. There are three α-helical domains in the protein denoted as I, II, and III that further divided into two subdomains A and B. These helical domains were identified from the crystal structure of HSA (PDB:1BM0, 2.5 Å) (33). These specific domains are targeted by rQTY code for rationale redesign. Since more ligand binding sites are present in A subdomains to B subdomains (34, 35), we conducted the substitutions primarily in B domains, namely IB, IIB, and IIIB, resulting in variants named HSA-IB^{rQTY}, HSA-IIB^{rQTY}, and HSA-IIIB^{rQTY}, respectively (Fig. 1 *A* and *B*). There are no significant changes in the pI values between the native HSA and its rQTY variants due to their low sequence variation rates (1.20 to 1.54%), whereas MWs decrease 0.12%, 0.12%, and 0.09% for HSA-IB^{rQTY}, HSA-IIB^{rQTY}, and HSA-IIIB^{rQTY} compared to the original HSA, respectively.

To evaluate the structural similarity between native HSA and rQTY variants, AlphaFold2 (36) was used to predicted the variant structures. As shown in Fig. 1*C*, HSA-IB^{rQTY}, HSA-IIB^{rQTY}, and HSA-IIIB^{rQTY} all attained heart-shaped conformations similar to the native protein, where redesigned domains were highlighted in green. Superpositions between rQTY variant predictions to the native HSA crystal structure were conducted using PyMOL alignment (*SI Appendix*, Fig. S1), and the RMSD values were all less than 1 Å over 585 residues (*SI Appendix*, Table S1). An additional TM-score (template modelling score) measure was also calculated (37), with high value of >0.97 suggesting conformational similarities. Sequence-dependent hydrophilicity for rQTY variants was predicted by the Hphob/Kyte & Doolittle Method using the ProtScale Software program (Fig. 1*D*), where notable increases in hydrophobicity were observed in rQTY substituted positions.

Both the native HSA and rQTY variants were expressed in *Escherichia Coli*. The purified recombinant proteins were analyzed using various instruments. As shown in Fig. 1*E*, SDS-PAGE gel showed protein bands between 65 kDa to 70 kDa. Circular Dichroism (CD) revealed the characteristic α-helical spectra with signature valleys at 208 nm and 222 nm, thus suggesting similar secondary structures of HSA and rQTY variants (Fig. 1*F*). The chemical structures were assessed using Fourier-transform infrared spectroscopy (FT-IR) (Fig. 1*G*). Characteristic bands including C-N stretching vibration (3,400 cm^{-1}), amide I band (1,700 to 1,600 cm^{-1}) attributed to the C=O stretch vibrations of the peptide linkages, the amide II band (1,600 to 1,490 cm^{-1}) derived from in-plane N-H bending, and amide III band (1,400 to 1,300 cm^{-1}) can be clearly observed in the spectra (38). These characterizations suggested that HSA^{rQTY} variants displayed highly similar molecular structures, structural composition and chemical structures compared to the native protein.

Fabrication of Self-Assembling HSA^{rQTY} Nanoparticles Without Organic Reagent. We next evaluated the self-assembling capability of amphiphilic HSA^{rQTY} into nanoparticles (Fig. 2*A*). Three types of HSA nanoparticles made from HSA-IB^{rQTY}, HSA-IIB^{rQTY}, and HSA-IIIB^{rQTY} were prepared by self-assembly at neutral pH without any organic reagent. Native HSA was treated using the same procedure as the control. In parallel, HSA and BSA nanoparticles were also prepared using the traditional antisolvent precipitation method (12, 39).

The morphology and particle size distribution of nanoparticles were studied using transmission electron microscopy (TEM) and dynamic light scattering. HSA-IB^{rQTY}, HSA-IIB^{rQTY}, and HSA-IIIB^{rQTY} nanoparticles were shown to be spherical in shape with particle average sizes of 151.9 ± 3.6 nm, 115.4 ± 0.7 nm, and 87.6 ± 2.3 nm, respectively, whereas no nanoparticles were observed in the native HSA group after undergoing the self-assembly process. Both HSA and BSA nanoparticles prepared by the antisolvent precipitation method also exhibited spherical

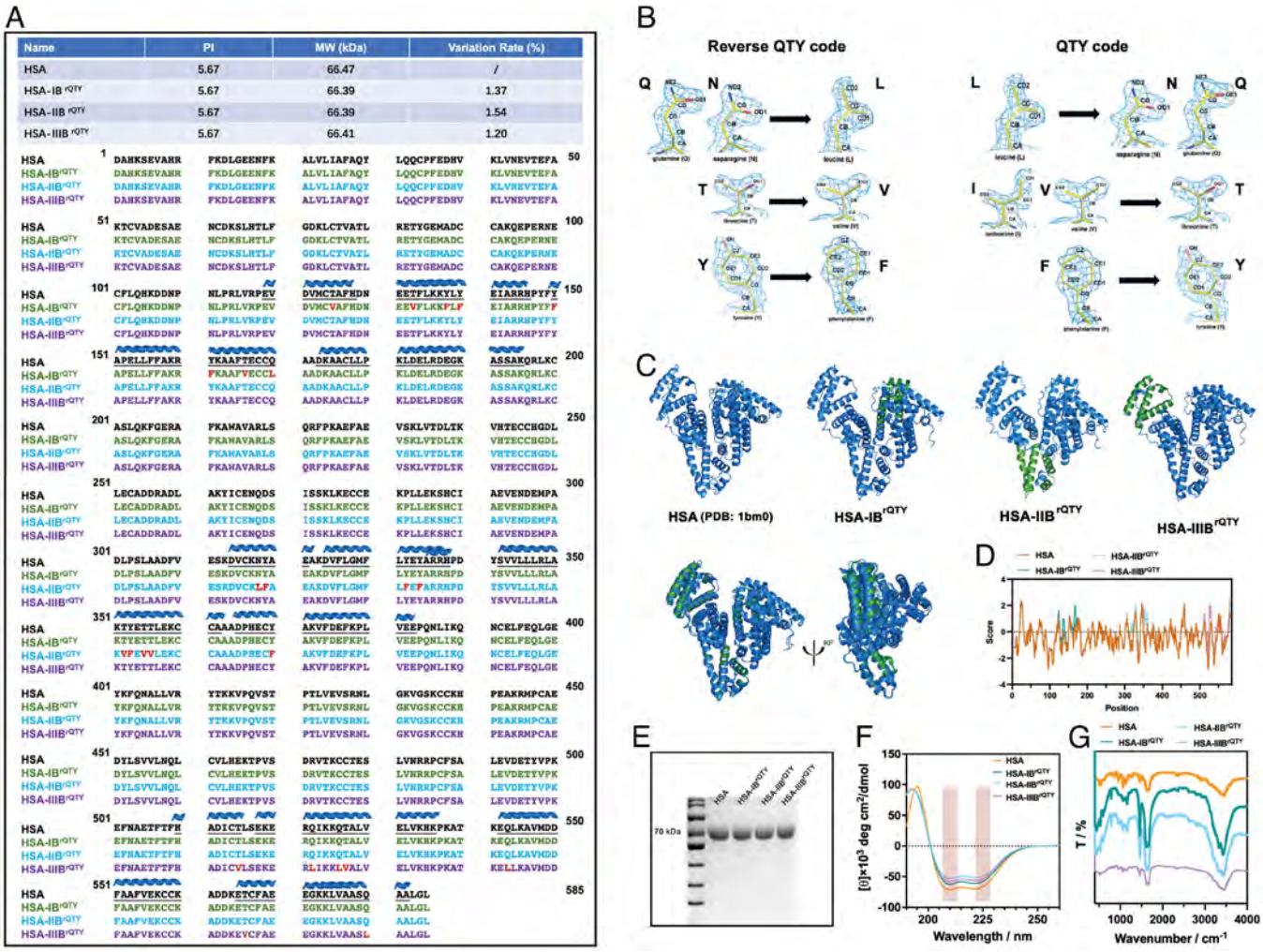

Fig. 1. The rQTY design and characterization of HSA proteins. (*A*) Sequence alignments of native HSA with HSA-IB^{rQTY}, HSA-IIB^{rQTY} and HSA-IIIB^{rQTY}. (*B*) Schematic illustration for the comparison between reverse-QTY code and QTY code. (*C*) Structure predictions of HSA-IB^{rQTY}, HSA-IIB^{rQTY}, and HSA-IIIB^{rQTY} using Alphafold2. The rQTY-modified regions are highlighted in green. The crystal structures of four proteins were superimposed. (*D*) Kyte-Doolittle hydrophobicity plot of native HSA and rQTY variants. (*E*) The SDS-PAGE showed the protein bands between 65 kDa to 70 kDa. (*F*) CD spectra of the characteristic α-helical spectra with signature valleys at 208 nm and 222 nm and (*G*) FT-IR spectra of native HSA, HSA-IB^{rQTY}, HSA-IIB^{rQTY}, and HSA-IIIB^{rQTY} proteins.

shape with sizes of ~100 nm, indicating that rQTY code designed amphiphilic HSA can be used to prepare nanoparticles through molecular self-assembly, which exhibited similar morphology and particle size distributions comparable to HSA and BSA nanoparticles that were fabricated by antisolvent precipitation method.

CMC is the main physicochemical parameter to determine the self-assembly scale for amphiphilic proteins (40), which was measured by pyrene method for three types of HSA^{rQTY} micelles (Fig. 2*B*) (41). The CMC of HSA-IB^{rQTY}, HSA-IIB^{rQTY}, and HSA-IIIB^{rQTY} is 5.68 μg/mL, 1.72 μg/mL, and 5.60 μg/mL, respectively, indicating the high stability of nanoparticles. Then, we tested the influence from ionic strength of solution on particle sizes of HSA-IB^{rQTY}, HSA-IIB^{rQTY}, and HSA-IIIB^{rQTY}, to verify that the hydrophobic interaction is the main driving force for self-assembly since higher iconic strength will enhance hydrophobic interactions and lead to larger particle sizes (Fig. 2*C*) (42, 43).

Indeed, the particle size of three types of rQTY-designed HSA nanoparticle increased with increasing concentrations of NaCl (Fig. 2*D*). Furthermore, the yields of HSA^{rQTY} nanoparticles were also counted (Fig. 2*E*). The numbers of nanoparticles decreased when concentrations of NaCl were higher than 100 mM, which was attributed to the increased particle size at same protein concentrations.

Generally, smaller CMC results in better stability of micelles. To ensure that the micelle structure is not destroyed when they enter the blood circulation through intravenous administration, it is necessary for micelles to have a low CMC value. Theoretically, higher hydrophobicity of micelle can be grafted with a lower CMC value, and the designed HSA-IIB^{rQTY} present the highest positive Grand average of hydropathicity score among the three domains (*SI Appendix*, Table S2). However, the scores are not proportional to nanoparticle diameters, perhaps due to the influence of other characteristics of proteins, such as steric hindrance. HSA molecules display a heart shape, and the prohibition of self-assembly of HSA-IB^{rQTY} maybe caused by the steric hindrance because that the rQTY designed region located at the concave side of HSA. Thus, larger HSA-IB^{rQTY} nanoparticle was observed compared to HSA-IIB^{rQTY} and HSA-IIIB^{rQTY} nanoparticles.

Induced denaturation of rQTY-designed HSA nanoparticles by self-assembly was also assessed (*SI Appendix*, Fig. S2). Turbidity experiments were performed as when proteins are denatured and aggregated, the turbidity of their solutions will increase (44, 45). In the present study, the turbidity of the solution of the rQTY-modified HSA nanoparticles was significantly lower than that of the BSA and HSA nanoparticles, implying that no denaturation was observed in the preparation of the designed

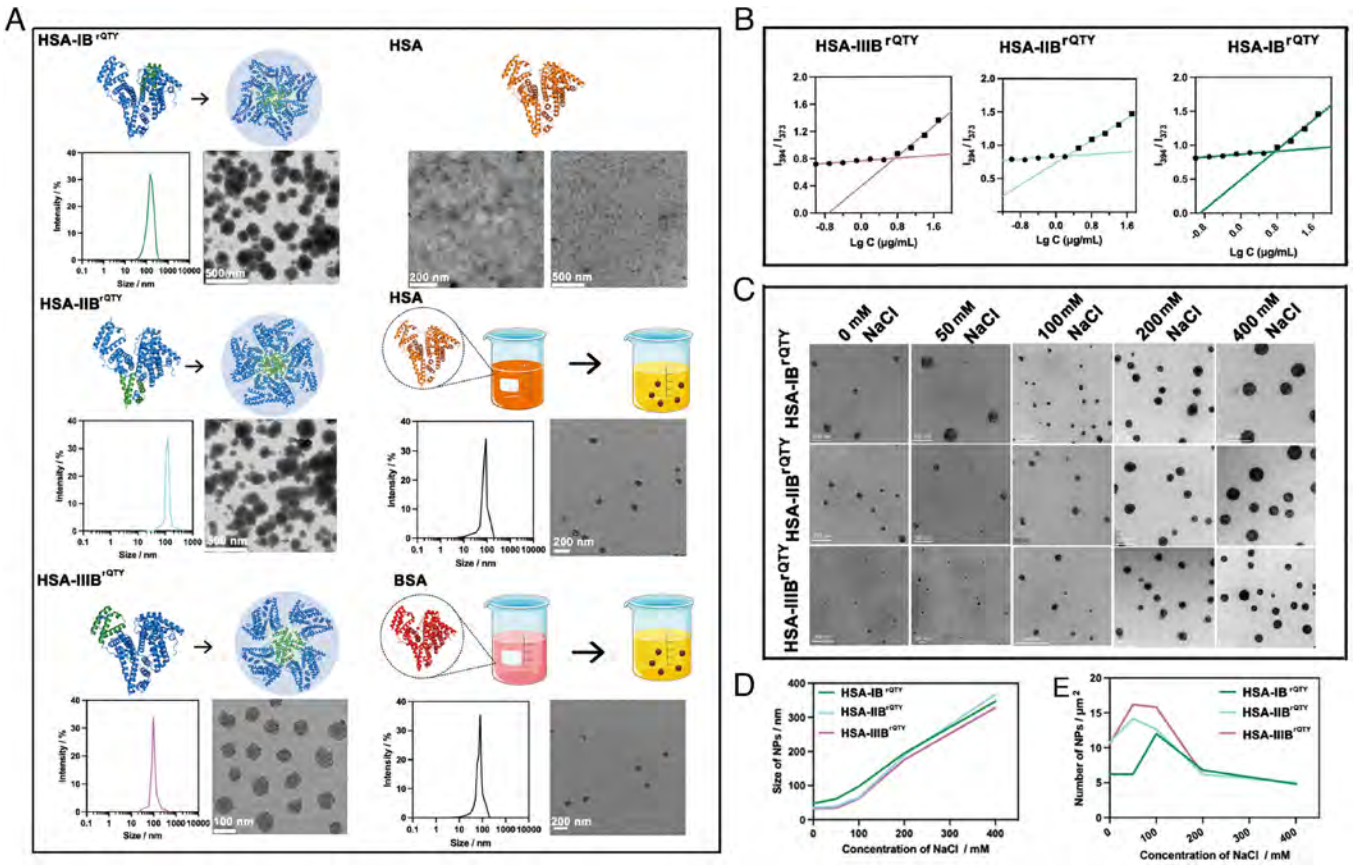

Fig. 2. Self-assembly of rQTY-designed HSA into nanoparticles. (*A*) Schematic of nanoparticle formation, particle size and TEM images of rQTY-designed HSA variants, native HSA and BSA nanoparticles. The rQTY-designed HSA can self-assemble into nanoparticles (*Left*), while no nanoparticle was observed in the native HSA group with the same fabrication procedure (*Right*). The concentrations of HSA^{rQTY}, HSA, and BSA were approximately 1.50×10^{-2} M. (*B*) Plots of absorbance for rQTY-designed HSA variants versus concentration (μg/mL) in logarithmic scale. The CMC of HSA-IB^{rQTY}, HSA-IIB^{rQTY}, and HSA-IIIB^{rQTY} is 5.68 μg/mL, 1.72 μg/mL, and 5.60 μg/mL, respectively, indicating the high stability of nanoparticles. The dotted line shows the CMC value. (*C*) TEM images, (*D*) particle size, and (*E*) number of rQTY-designed HSA nanoparticles under different ionic strength conditions.

self-assemble HSA nanoparticle. In comparison, induced denaturation of HSA^{rQTY} nanoparticles still exhibited much lower turbidity compared to HSA and BSA nanoparticles, which helped the designed HSA to largely retain their native conformations and capability to be uptake by receptor-mediated pathways. With that, the rQTY code has proven to be a powerful tool for the design of hydrophobic functional proteins with well-defined interfaces.

Drug Uptake and Release Capability of HSA^{rQTY} Nanoparticles. To combat tumor, effective antitumor drug uptake, sustained release and biocompatibility of nanoparticles are also required for tumor therapies. Since native HSA and BSA are highly hydrophilic, that cannot self-assemble into nanoparticles by the same protocol of HSA^{rQTY} nanoparticles. Furthermore, no drug was detected in the unself-assembled HSA and BSA samples, and few study used the single HSA or BSA to treat cancer cells as their low antitumor efficiency. Therefore, the DOX-loaded HSA and BSA nanoparticles were fabricated using the common desolvation method to compare their drug delivery properties with HSA^{rQTY} nanoparticles. The drug loading and release profiles of HSA^{rQTY} nanoparticles were determined using an anthracycline antitumor antibiotic named DOX as the model (46). DOX has been widely used to treat various tumors by inhibiting the synthesis of RNA and DNA (47, 48). DOX was directly mixed with HSA^{rQTY} solutions, which was likely entrapped into the hydrophobic region of HSA^{rQTY} nanoparticles during their formulation (Fig. 3*A*). The drug loading in HSA-IB^{rQTY}, HSA-IIB^{rQTY}, and HSA-IIIB^{rQTY} nanoparticles was 23.31 ± 2.06%, 21.09 ± 1.44%, and 19.26 ± 1.75%, respectively (*SI Appendix*, Table S3).

Meanwhile, doxorubicin-loaded HSA and BSA nanoparticles were also prepared by the traditional antisolvent precipitation method, and the doxorubicin loadings of HSA and BSA nanoparticles were 4.35 ± 0.62% and 2.67 ± 0.74%, respectively. Significantly improved drug loadings were observed for HSA^{rQTY} nanoparticles prepared through self-assembly. The doxorubicin release profiles at pH 7.4 and pH 6.8 were then determined to evaluate their performance both in normal human blood (pH 7.35 to 7.45) (49) and in tumor microenvironment with weak acidity (50–52). As expected, all HSA nanoparticles exhibited sustained doxorubicin release within 168 h (Fig. 3*B*). The cumulative releases of doxorubicin from HSA^{rQTY} nanoparticles are approximately 50% at 48 h, 75% at 96 h, and 90% at 144 h at pH 7.4, with relatively faster release rate at pH 6.8. In contrast, approximately 75% of doxorubicin was released from HSA and BSA nanoparticles within 48 h. The HSA^{rQTY} nanoparticles also took significantly longer time to release 50% of the drug enclosed especially at pH 6.8 (Fig. 3*C*). The profiles suggested that HSA^{rQTY} nanoparticles exhibited better performance in continuous drug release compared to nanoparticles prepared by antisolvent precipitation method of native HSA.

We next evaluated the cytotoxicity of HSA-IB^{rQTY}, HSA-IIB^{rQTY} and HSA-IIIB^{rQTY} nanoparticles in HEK293T, L929, 4T1, A549 and Human Umbilical Vein Endothelial Cells (HUVEC) cells using CCK-8 analysis (Fig. 3*D*) and live and dead cell staining (Fig. 3*E* and *SI Appendix*, Figs. S3–S5) (53, 54). The relative

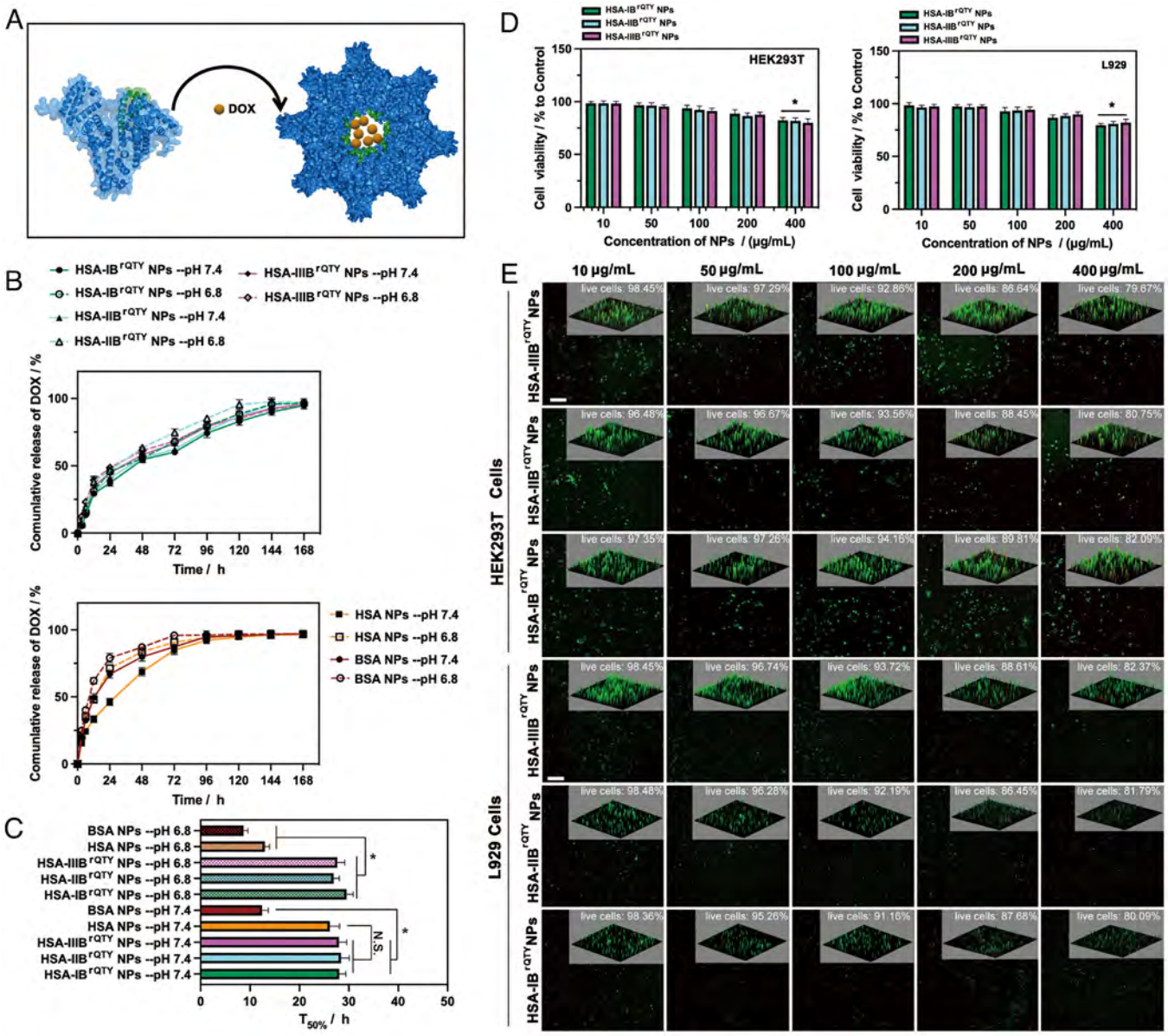

Fig. 3. In vitro drug release test and cytotoxicity analysis of rQTY-designed HSA nanoparticles (NPs). (*A*) The diagram of doxorubicin (DOX)-loaded rQTY-designed HSA nanoparticles, brown particles represent the drug and the blue area indicates the hydrophobic domains which interact with drugs by hydrophobic interactions. (*B*) In vitro release profiles of doxorubicin from HSA-IB^{rQTY}, HSA-IIB^{rQTY}, HSA-IIIB^{rQTY}, HSA and BSA nanoparticles at different pH conditions, $n = 5$. (*C*) Time required for 50% drug release from different albumin nanoparticles under different pH conditions, $n = 5$. The viability of HEK293T and L929 cells after co-incubation of HSA-IB^{rQTY}, HSA-IIB^{rQTY}, HSA-IIIB^{rQTY} nanoparticles for 24 h, $n = 3$. (*D*) The viability and (*E*) staining results of live and dead cells of HEK293T and L929 cells after co-incubation of HSA-IB^{rQTY}, HSA-IIB^{rQTY}, HSA-IIIB^{rQTY} nanoparticles for 24 h. The scale bar is 100 μm. Graphs are presented as means ± SD, and the statistical significance was calculated by One-way ANOVA followed by a post hoc Tukey's multiple comparison test. *$P < 0.05$.

viability of cells remained above 80% when the concentration of the HSA^{rQTY} nanoparticles reached 400 μg/mL. Very high numbers of live cells can be seen in cells at nanoparticle concentrations below 400 μg/mL. Our results suggested good biocompatibility of fabricated rQTY-designed HSA nanoparticles.

Cellular Internalization of HSA^{rQTY} Nanoparticles through the GP60 and SPARC-Mediated Pathway. It was previously reported that the uptake of denatured HSA was less affected by the GP60 pathway inhibitor. However, it is significantly reduced by denatured albumin receptor inhibitors (18). We then benchmarked the cellular internalization capacity of HSA^{rQTY} nanoparticles through receptor-mediated transport by GP60 and SPARC (Fig. 4*A*). Immunofluorescence experiments were performed, and the results showed that that GP60 receptors are highly expressed in HUVEC, but almost absent in HEK293T, L929, 4T1 and A549 cells (Fig. 4*B*). HUVECs are the commonly used cell model in vascular endothelial cell experiments, such as hypoxia, inflammation, oxidative stress, infection response, normal or tumor-associated angiogenesis (18, 55). We also performed immunofluorescence staining of tumor cells 4T1, A549, HEK293T, L929 and HUVECs for SPARC (Fig. 4*C*). The nucleus is in blue and the SPARC is in red, where SPARC was found significantly expressed in both tumor cells 4T1 and A549, but not in normal cells HEK293T, L929 and HUVEC (12).

Since HSA-IB^{rQTY} nanoparticles have the best drug-loading capacity, therefore, HSA-IB^{rQTY} nanoparticles were selected to carry out subsequent cell and mice experiments. Fluorescein isothiocyanate (FITC)-labeled nanoparticles were co-incubated with GP60 inhibitor of methylated-β-cyclodextrin to determine the

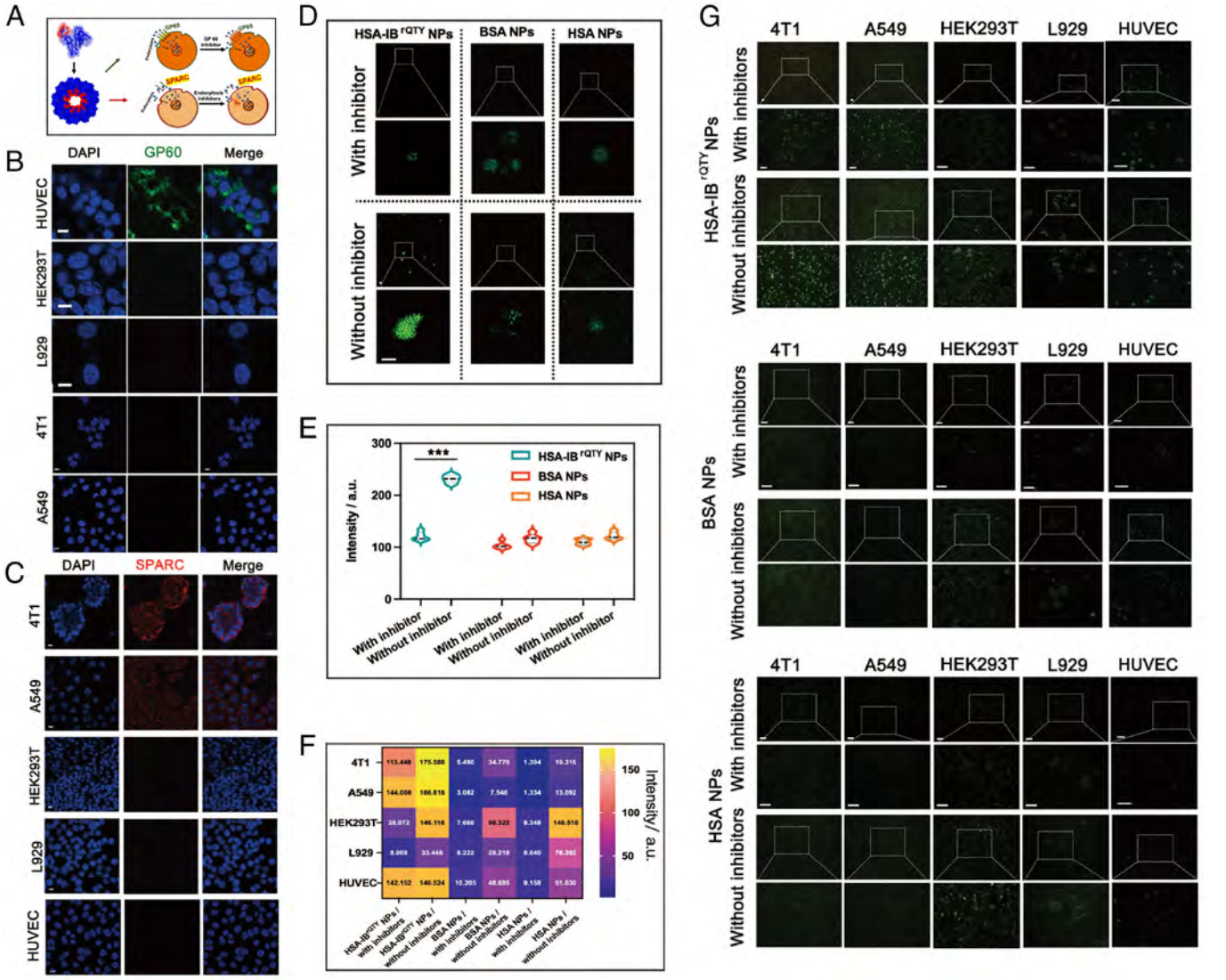

Fig. 4. Cellular uptake and transport pathways of rQTY-designed HSA nanoparticles (NPs). (*A*) Schematic representation of the cellular uptake of HSA nanoparticles via GP60 and SPARC-mediated pathways. Inhibitors and cells were co-incubated to investigate the effect of GP60 and SPARC expression on the uptake of HSA nanoparticles. (*B*) The expression of GP60 in HUVEC, HEK293T, L929, 4T1, and A549 cells (Scale bar, 10 μm.). (*C*) The SPARC expression in 4T1, A549, HEK293T, L929 and HUVEC cells (Scale bar, 10 μm.). (*D*) Representative fluorescence imaging (Scale bar, 10 μm.) and (*E*) quantitative analysis on the uptake of FITC-HSA-IB^{rQTY}, BSA and HSA nanoparticles by HUVEC after incubation with or without the GP60 inhibitor. 4T1, A549, 293T, L929 and HUVEC cells were incubated with FITC-HSA-IB^{rQTY}, BSA and HSA nanoparticles. (*F*) quantitative analysis and (*G*) representative fluorescence imaging for the uptake of FITC-HSA-IB^{rQTY}, BSA and HSA nanoparticles by cells after incubation with or without endocytosis inhibitors. (Scale bar, 100 μm.) $n = 5$, graphs are presented as means ± SD, and the statistical significance was calculated by One-way ANOVA followed by a post hoc Tukey's multiple comparison test. ***$P < 0.001$. a.u., arbitrary units.

effect of GP60 expression in HUVECs on their cellular uptake (Fig. 4*D*) (56). A stronger fluorescence intensity was observed in the HSA-IB^{rQTY} nanoparticles group compare to those in HSA and BSA nanoparticles, indicating higher nanoparticle uptake into HUVECs. The number of HSA-IB^{rQTY} nanoparticles entering the cells was significantly reduced after co-incubation with methylated-β-cyclodextrin, while only slight reduction in fluorescence intensity was observed for HSA and BSA nanoparticles (Fig. 4*E*) ($P < 0.001$). Besides, we have also done the same experiment in HEK293T, L929, 4T1 and A549 cells. The results of fluorescence density of observations (*SI Appendix*, Fig. S6), and no significant difference in the number of nanoparticles entering the cells after co-incubation with or without methylated-β-cyclodextrin because that GP60 receptors were absent in 4T1, A549, HEK293T and L929 cells. These results suggested that the internalization of HSA-IB^{rQTY} nanoparticles into HUVECs relied heavily on GP60 receptor-mediated transport, which was not the case for HSA and BSA nanoparticles.

Uptakes of HSA-IB^{rQTY}, HSA and BSA nanoparticles by tumor cells 4T1 and A549 and normal cells HEK293T, L929, and HUVEC are shown in Fig. 4 *F* and *G*, as well as the fluorescence intensity of cells after incubation with or without the endocytosis inhibitors, namely chlorpromazine (15 μg/mL), amiloride (75 μg/mL), and MβCD (7.5 mM) (57). The fluorescence intensities of 4T1 and A549 cells are higher compared to those of HEK293T, L929 and HUVEC cells for HSA-IB^{rQTY} nanoparticles, with or without endocytosis inhibitors. Yet adding endocytosis inhibitors significantly decreased the fluorescence intensities of 4T1 and A549 cells, by approximately 35.42% and 13.25%, respectively. The numbers are ~80% and ~75.76% for HEK293T and L929 cells, respectively. However, for HUVEC cells, there was hardly any decrease in fluorescence density before and after addition of the inhibitors, and this is due to the fact that despite addition of the cytokinesis inhibitors, HSA-IB^{rQTY} nanoparticles could still enter HUVEC cells via the GP60 pathway. All above results suggested that HSA-IB^{rQTY} nanoparticles uptake happen both in tumor and

normal cells by the SPARC-mediated pathway, while endocytosis inhibitors more significantly inhibit their accumulation in HEK293T and L929 cells. In contrast, the fluorescence intensity of labeled BSA and HSA nanoparticles were less than ~20% of those for HSA-IB^{rQTY} nanoparticles in corresponding cells, indicating that the latter has greater potential in tumor-targeting delivery. Moreover, the accumulation of ~60% BSA to ~94.33% HSA nanoparticles were inhibited by combined endocytosis inhibitors, showing that endocytosis rather than SPARC-mediation is the predominant pathway for BSA and HSA nanoparticles. The above results strongly suggested that the designed HSA-IB^{rQTY} nanoparticles provide more efficient cellular internalization in HUVECs and tumor cells 4T1 and A549 through GP60 and SPARC-mediated pathways.

Flow cytometry experiments were also carried out to evaluate the cellular uptake and transport pathways of rQTY-designed HSA nanoparticles. The FITC labelled HSA-IB^{rQTY} nanoparticles, BSA nanoparticles and HSA nanoparticles were co-cultured with cells for 24 h, respectively, and cells were then collected for flow experiments. Since the results of immunofluorescence analysis indicated that GP60-mediated pathway take a critical role in the cellular uptake of HSA nanoparticles into HUVEC cells, flow cytometry analysis was firstly performed to evaluate the entrance of HSA-IB^{rQTY} nanoparticles, BSA nanoparticles and HSA nanoparticles into HUVEC cells. The HUVECs with mean fluorescence intensity exceeded 130,000 a.u. after co-culture with FITC-labeled HSA-IB^{rQTY} nanoparticles (Fig. 5 *A* and *B*), while, the mean fluorescence intensity of HUVECs was approximately 50,000 a.u. in the BSA nanoparticles and HSA nanoparticles groups. More importantly, the shape reduction of fluorescence intensity of HUVECs incubated with HSA-IB^{rQTY} nanoparticles was noted when the GP60 inhibitor was added, suggesting that HSA-IB^{rQTY} nanoparticles are more dependent on GP60-mediated pathway to enter HUVEC than on other cellular uptake pathways. Furthermore, we also assessed the cellular internalization of different albumin nanoparticles into 4T1, A549, HEK293T and L929 cells after co-culture with or without GP60 inhibitor using flow cytometry analysis (*SI Appendix*, Figs. S7–S12). The higher fluorescence intensity can be noted in 4T1 and A549 cells compare to that in the HEK293T and L929 cells, which can be explained that albumin nanoparticles can enter tumor cells via SPARC pathway. Besides, The 4T1 and A549 cells with mean fluorescence intensity exceeded 80,000 a.u. after co-culture with FITC-labeled HSA-IB^{rQTY} nanoparticles, which are higher than that treated with BSA and HSA nanoparticles (approximately 30,000 a.u.), indicating the designed HSA-IB^{rQTY} nanoparticles showed more efficient cellular internalization. Meanwhile, no significant difference in fluorescence intensity was observed in four cells when the different albumin nanoparticles incubated with or without GP60 inhibitor, because that 4T1, A549, HEK293T and L929 cells do not express GP60 receptors.

Moreover, we also assessed the cellular internalization efficiency of different albumin nanoparticles into tumor cells via the SPARC using flow cytometry analysis. We observed that the mean fluorescence intensities of cells including 4T1, A549, HEK293T, L929 and HUVEC cells were above 50,000 a.u. after incubation of HSA-IB^{rQTY} nanoparticles (Fig. 5 *C* and *D*), in particular, the mean fluorescence intensity of tumor cells 4T1 and A549 cells exceeded 80,000 a.u. While the mean fluorescence intensity of normal cells HEK293T and L929 cells were approximately 10,000 a.u. after the addition of inhibitors of endocytosis, in contrast, the mean fluorescence intensity of tumor cells 4T1, A549 and HUVEC cells remained above 50,000 a.u. This is due to the high expression of SPARC and GP60 receptor on tumor cells and HUVECs, respectively. Furthermore, the mean fluorescence intensity of these five types of cells was significantly reduced after co-incubation of endocytosis inhibitors with BSA or HSA nanoparticles (*SI Appendix*, Figs. S13–S16) ($P < 0.01$), suggesting that the cellular internalization of BSA and HSA nanoparticles are highly depended on the endocytosis. Taken together, these results provided strong evidence that the designed HSA-IB^{rQTY}

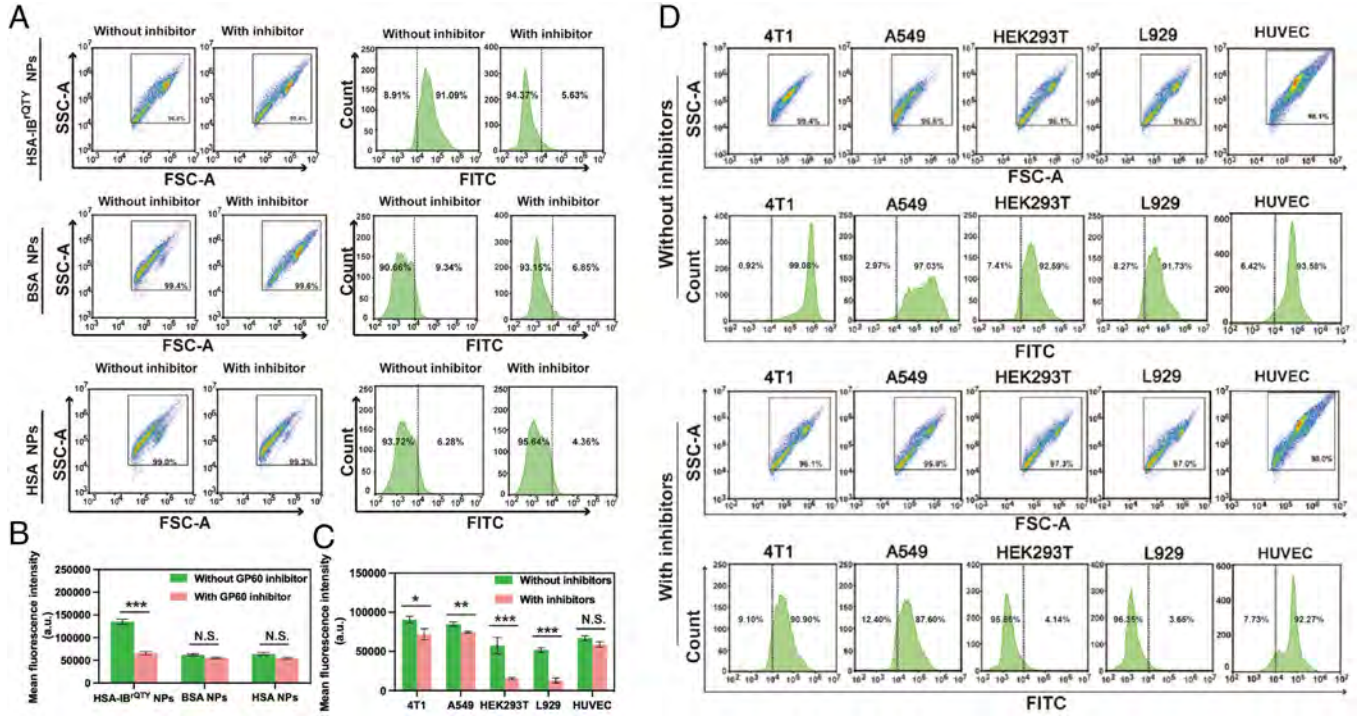

Fig. 5. Flow cytometry assay for cellular uptake of different albumin nanoparticles (NPs). (*A*) Flow cytometry and (*B*) quantitative analysis of cell internalization of FITC-HSA-IB^{rQTY} NPs, BSA NPs, and HSA NPs after coincubation of HUVEC without or with GP60 inhibitor. (*C*) Quantitative analysis and (*D*) flow cytometry of cell internalization of FITC-HSA-IB^{rQTY} NPs after coincubation of various cells without or with endocytosis inhibitors.

nanoparticles can be efficiently internalized into HUVECs and tumor cells through receptor-mediated pathways.

Antitumor Efficacy of HSA^{rQTY} Nanoparticles. To determine the therapeutic effect of doxorubicin-loaded HSA-IB^{rQTY} nanoparticles, an animal model was built with tumor-bearing BALB/c mice. The groups of control, free doxorubicin, DOXIL®, doxorubicin@BSA nanoparticles, doxorubicin@HSA nanoparticles, and doxorubicin@HSA-IB^{rQTY} nanoparticles were established parallelly to compare their therapeutic effects of different nanoparticles. Subcutaneous injections of 1×10^7 4T1-luc cells were conducted at the right flank of each mouse (Fig. 6*A*) (51), and drug-treatments were initiated when tumors grew to about 50 mm^3, which took about 5 d. As shown in Fig. 6 *B–D*, the tumor sizes in the doxorubicin@HSA-IB^{rQTY} group were significantly smaller than in other experimental groups after the treatment (*SI Appendix*, Fig. S17) ($P < 0.01$). The doxorubicin@BSA and doxorubicin@HSA nanoparticles showed observable therapeutic effect compared to the control and free doxorubicin groups. It is apparent that more efficient inhibition in tumor growth were observed in the doxorubicin@HSA-IB^{rQTY} group. The conclusion cross-referenced well with changes in tumor growth rate (Fig. 6*E*), survival time (>70 d) (Fig. 6*F*), and body weight (Fig. 6*G*) of the tumor-bearing mice in each experimental group.

Statistical significance was also established for the tumor size and volume measurements in each group. The body weights of tumor-bearing mice in the control and free doxorubicin group significantly decreased at the late stage of treatment, indicating health deterioration in mice ($P < 0.01$). Mice treated with doxorubicin@BSA or doxorubicin@HSA nanoparticles showed neither significant loss or gain in their body weight. In comparison, mice in the doxorubicin@HSA-IB^{rQTY} group continued to gain weight in the later stage of treatment. Moreover, tumor-bearing mice in the doxorubicin@HSA-IB^{rQTY} group survived significantly longer than in other experimental groups ($P < 0.01$). Similarly, the tumor growth rate of mice treated with doxorubicin@HSA-IB^{rQTY} nanoparticles was significantly lower than those in other experimental groups ($P < 0.001$). These results suggested that doxorubicin@HSA-IB^{rQTY} nanoparticles not only can effectively inhibit tumor growth in the BALB/c mouse model, but also exhibited superior performance to nanoparticle systems prepared through traditional means.

In order to comprehensively determine the therapeutic efficacies, tumor tissues from mice in each experimental group were sectioned and stained to image relevant indicators. Tumors removed at day 42 showed consistent size differences with in vivo fluorescence imaging results (Fig. 6*H*). The volume (Fig. 6*I*) and weight (Fig. 6*J*) of isolated tumors after the treatments were also measured. The samples from the doxorubicin@HSA-IB^{rQTY} group were significantly smaller than other experimental and control groups ($P < 0.001$).

We then performed the H&E staining and TUNEL staining on tumor tissues (Fig. 6*K*). Sparsest tumor cells were observed in mice with doxorubicin@HSA-IB^{rQTY} nanoparticle treatment, followed by doxorubicin@BSA and doxorubicin@HSA nanoparticles, while lesser tumor cell reduction in the free doxorubicin group, and most dense tumor cells in the control group, were observed (Fig. 6*L*). The same conclusion can be drawn from the TUNEL staining results. It can be clearly seen that most apoptotic cells (red) were found in the tumor tissue after the treatment of doxorubicin@HSA-IB^{rQTY} nanoparticles. Doxorubicin@BSA and doxorubicin@HSA nanoparticles showed observable but inferior tumor inhibition effects as compared to doxorubicin@HSA-IB^{rQTY} nanoparticles. We next assessed the number of white blood cells (Fig. 6*M*) and monocytes (Fig. 6*N*) in the blood of tumor-bearing mice, which reflected the severity of the disease (58). The results showed significantly lower number of white blood cells and monocytes in mice of the doxorubicin@HSA-IB^{rQTY} group compared with other groups ($P < 0.001$), demonstrating its better therapeutic efficacy from the perspective of biomarkers in blood. These results were consistent with in vivo characterizations, both of which proved doxorubicin@HSA-IB^{rQTY} nanoparticles a superior carrier for continuous release of drug within the tumor.

Receptor-Mediated HSA^{rQTY} Nanoparticle Uptake and Delivery for Active Tumor Targeting. To reveal the underlying mechanism for the superior antitumor therapeutic performance of HSA^{rQTY} nanoparticles as compared to doxorubicin@BSA and doxorubicin@HSA nanoparticles, we investigated their enrichments in tumor and major organs after 2 h of the tail-vein injection. IR783 was used to label BSA, HSA and HSA-IB^{rQTY} for easier imaging (59). Tumors and major organs including heart, liver, spleen, lung and kidney were removed from mice in each experimental group and subjected to fluorescence imaging under a live imager (Fig. 7*A*). The results of ex vivo imaging showed that doxorubicin@HSA-IB^{rQTY} nanoparticles exhibited strong enrichments in tumors but only slight residues in other major organs. Although doxorubicin@BSA and doxorubicin@HSA nanoparticles were enriched in tumors, they also significantly accumulated in the lung and liver (Fig. 7*B*). The preferential enrichment of doxorubicin@HSA-IB^{rQTY} nanoparticles in the tumor implied that redesigned doxorubicin@HSA-IB^{rQTY} nanoparticles have better tumor-targeting capability compared to traditional delivery systems.

Furthermore, to verify the receptor-mediated doxorubicin@HSA-IB^{rQTY} nanoparticle delivery in vivo, we performed simultaneous immunofluorescence on CD31 and GP60. CD31 and GP60 are both expressed in vascular endothelial cells and used as biomarkers of the cells. Consequently, overlapping distributions of GP60 and CD31 were observed in immunofluorescence figures, co-localization analysis and fluorescence density distribution maps (*SI Appendix*, Fig. S18). The higher expression of CD31 and GP60 were found in the control group due to vigorous tumor growth and more neovascularization. Reduced expressions were observed in the free doxorubicin group, while more significant decreases were noted in nanoparticle groups. The doxorubicin@HSA-IB^{rQTY} group exhibited the lowest level of CD31 and GP60 compared to other groups, indicating a stronger inhibitory effect on tumor angiogenesis.

We then investigated the distribution of doxorubicin and doxorubicin-loaded nanoparticles in tumor tissues by co-localization doxorubicin with SPARC and GP60 (Fig. 7 *C–F* and *SI Appendix*, Figs. S19–S21). The higher red fluorescence intensity was observed in doxorubicin@HSA-IB^{rQTY} nanoparticles compared to other groups, and the co-localization results of SPARC and doxorubicin suggested higher efficacy for drug delivery into tumor cells from HSA^{rQTY} nanoparticles, and the significant decrease in SPARC expression in doxorubicin@HSA-IB^{rQTY} nanoparticle group was attributed to its excellent antitumor effect. Similar results were also observed when doxorubicin and doxorubicin-loaded nanoparticles were co-localized with GP60 expressed on tumor cells, which suggested the GP60 receptor was involved in the transcytosis of doxorubicin@HSA-IB^{rQTY} nanoparticles.

Finally, to evaluate the biosafety of the nanoparticles, their toxicity to major organs (including heart, liver, spleen, lung and kidney) and tissues (muscle around tumor, gastric fundus, gastroduodenum, gastric pylori, intestine) of tumor-bearing mice with different formulations was determined by H&E staining (*SI Appendix*, Fig. S22). The doxorubicin@HSA-IB^{rQTY} nanoparticles showed no significant

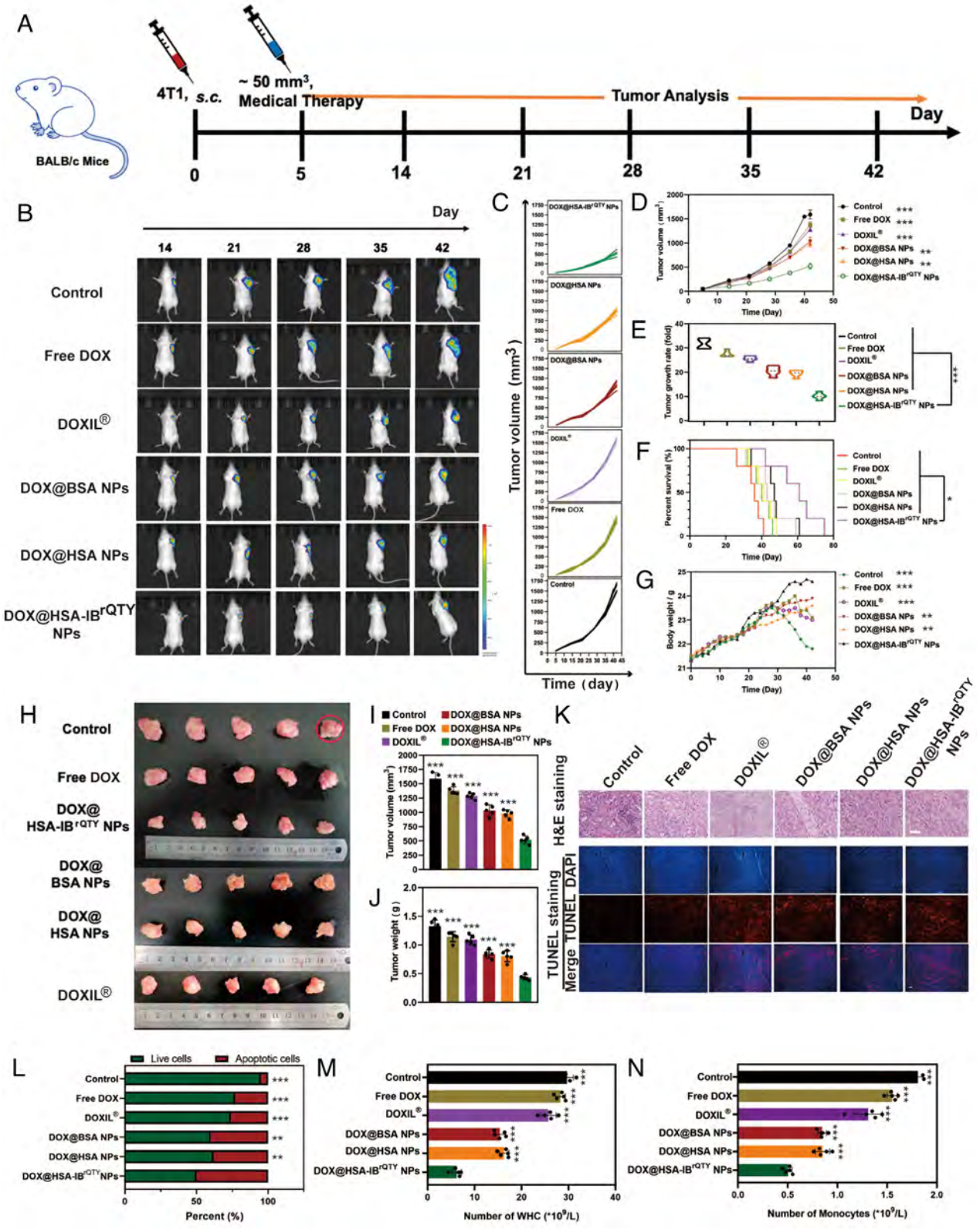

Fig. 6. HSA^{rQTY} nanoparticles (NPs) provided superior antitumor effect. (*A*) Timeline for the therapeutic process. Mice were administrated with different nanoparticles or doxorubicin through the tail vein 5 d post 4T1 tumor cells implantation. (*B*) Representative in vivo fluorescence imaging of tumor-bearing mice during the treatments of doxorubicin (DOX) and albumin nanoparticles or DOXIL® at 14, 21, 28, 35, and 42 d. (*C*) Tumor growth curves, (*D*) mean tumor growth curves, (*E*) tumor growth rate, (*F*) Kaplan–Meier survival curves, and (*G*) body weight change of tumor-bearing mice that received various treatments. (*H–J*), Mice were killed on 42 d and tumors were collected. (*H*) The tumor images, (*I*) tumor volume and (*J*) tumor weight of tumor-bearing mice after different treatments. The red circle highlighted tumor indicates that the mice were dead by 40 d in the control group. (*K*) Representative H&E, TUNEL staining and (*L*) quantitative analysis on the % of apoptotic cells of tumor sections in the tumor-bearing mice in different groups at 42 d. (The scale bar is 100 μm.) (*M*) Level of the white blood cells and (*N*) monocytes detected in different groups of tumor-bearing mice at 42 d. Scale bar, 100 μm, all data are presented as means ± SD, and $n = 5$. The statistical significance was calculated by one-way ANOVA followed by a post hoc Tukey's multiple comparison test. *$P < 0.05$, **$P < 0.01$, ***$P < 0.001$, *vs* doxorubicin@HSA-IB^{rQTY} group.

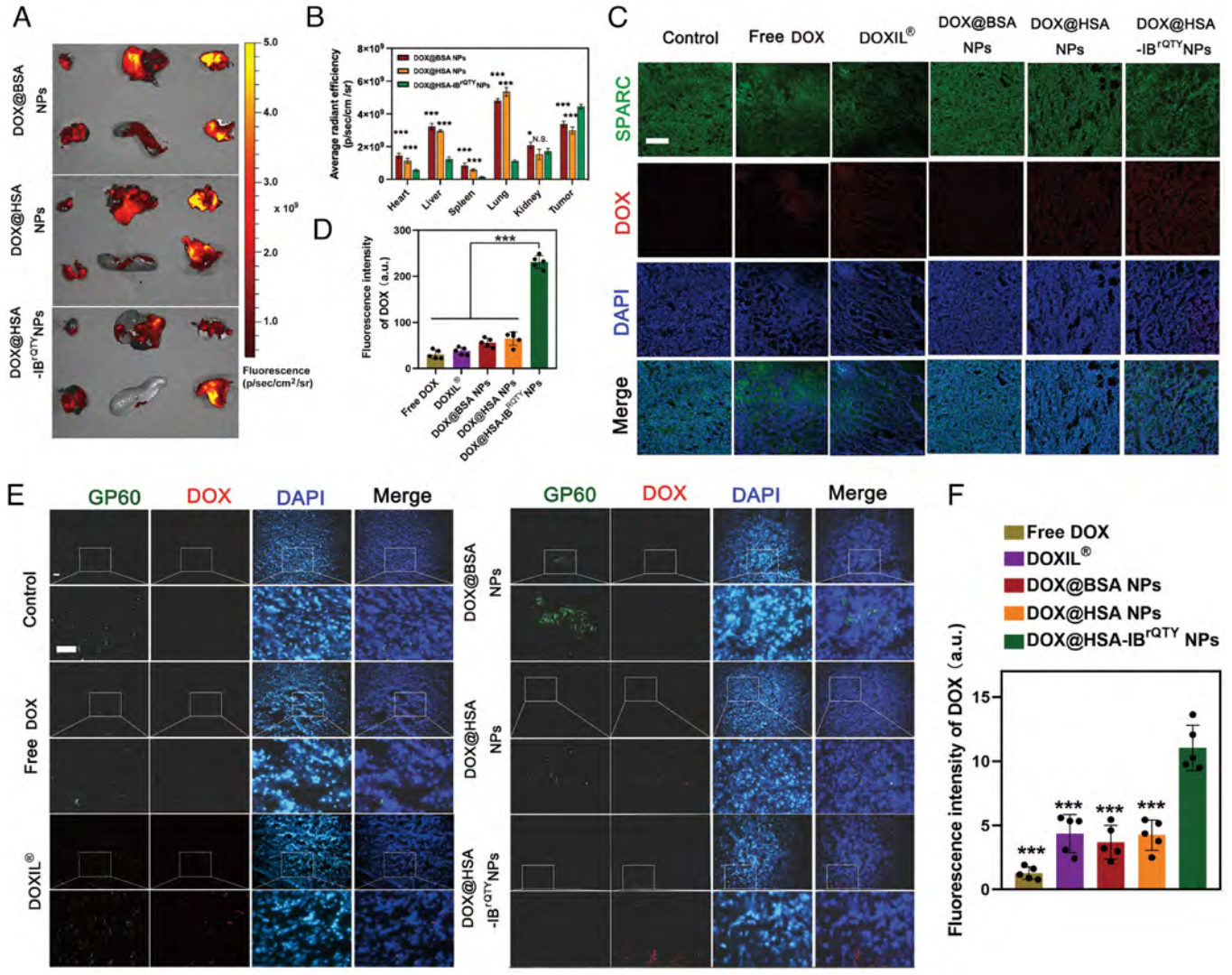

Fig. 7. In vivo distribution and biocompatibility of rQTY-designed HSA nanoparticles (NPs). (*A*) Ex vivo fluorescence imaging of main organs and tumor of the tumor-bearing mice at 2 h after the administration of doxorubicin (DOX)@BSA nanoparticles, doxorubicin@HSA nanoparticles and doxorubicin@HSA-IB^{rQTY} nanoparticles. (*B*) Quantification of ex vivo fluorescence images of main organs and tumor (means ± SD, $n = 5$). (*C*) Representative immunofluorescence and quantitative analysis (*D*) of SPARC and its colocalization with doxorubicin or doxorubicin-loaded nanoparticles. (*E*) Representative immunofluorescence and (*F*) quantitative analysis of GP60 and its colocalization with doxorubicin or doxorubicin-loaded nanoparticles. Scale bar, 100 μm, all data are presented as means ± SD, and $n = 5$. The statistical significance was calculated by one-way ANOVA with a Tukey post-hoc test. *$P < 0.05$; **$P < 0.01$; ***$P < 0.001$, vs. doxorubicin@HSA-IB^{rQTY} group. a.u., arbitrary units.

toxicity to major organs and tissues, while doxorubicin@BSA nanoparticles and doxorubicin@HSA nanoparticles presented some hepatotoxicity.

Discussion

HSA is one of the most abundant soluble proteins in human plasma, and thus HSA has attracted wide interests in drug delivery applications. However, the chemical modifications of HSA were required for drug conjunctions and delivery. The structure of HSA and their cellular transport pathways were reported to be changed by organic phase reactions, which added additional complexity into the fabrication of HSA-based carrier systems (19, 20). The redesign of HSA's primary sequence is an alternative approach to endow it with new functions and to promote protein self-assembly, so as to enable them as more capable drug delivery systems with increased drug loading.

The QTY Code and the Reverse QTY Code. The QTY code is a very simple and versatile protein design tool, which is based on 1.5 Å electron density maps of similar amino acids, for example, L:N/Q; V/I:T; F:Y (31, 32). The QTY code has been successfully used to design several types of integral membrane proteins including GPCRs (25, 26), cytokine receptors (60), glucose transporters (61), solute carrier transporters (62), by pairwise residue substitutions in the transmembrane region because nature has already evolved 3 distinct chemical types of alpha-helix including I) hydrophilic, II) hydrophobic, and III) amphiphilic types (63). It is believed that QTY code is reversibly applicable due to their unique structural correlation between polar and nonpolar amino acids. We here demonstrated the first example of designing towards defined hydrophobicity using the reverse-QTY rule, namely the rQTY code. The rationale aligns well with HSA's requirement for preferential association to self-assemble into functional nanoparticles and the design of a hydrophobic binding interface.

HSA-IB^{rQTY} as the Specific Drug Delivery System. The domain structure of HSA and its important functional sites were considered including multiple binding sites of foreign molecules, such as chemical compounds, fatty acids, and metal ions, as well

as the crucial Sudlow sites I and II located in subdomain IIA and subdomain IIIA, respectively (64). Thus, the three B substructure regions were targeted for rQTY code modification. Furthermore, GP60 and SPARC are key mediators for the transport of HSA-based drug delivery systems to tumors, so the binding sites of HSA/GP60 and HSA/SPARC were also avoided in the redesign. A previous study indicated that the albumin-binding domain of SPARC was located at residues 209 to 223 at the C-terminal domain (65). While there was no prior report on the location of binding sites in HSA toward GP60, our study showed a strong correlation between the GP60 receptor and the transcytosis of doxorubicin@HSA-IB^{rQTY} nanoparticles, suggesting functional sites preservation. Their interaction mechanisms can be further investigated through molecular docking in explicit solvents and site-specific mutagenesis. The similar approach was used to investigate the interaction mechanism of FcRn—albumin complex, which is a prerequisite for FcRn-dependent recycling and half-life regulation of albumin (66).

Delivery through the specific GP60 and SPARC-Mediated Pathways. Amongst the three designed variants, HSA-IB^{rQTY} showed the best cellular uptake and antitumor properties investigation because of its high drug loading capacity. The rQTY designed variant has shown superior biosafety, uptake and release profiles, antitumor efficacies and cell-targeting properties in all experimental sets due to its well-controlled mechanistic pathways. Compared with the HSA and BSA nanoparticles fabricated using the traditional antisolvent precipitation method, the in vitro and in vivo transport of HSA-IB^{rQTY} nanoparticles uses the specific GP60 and SPARC-mediated pathways rather than non-specific endocytosis, which were largely negated by protein denaturation in organic solvents during the preparation of drug-HSA conjugation reported from a previous study (18).

In summary, we demonstrated an efficient approach to design the amphiphilic HSA proteins using the rQTY code. The designed amphiphilic HSA exhibited strong self-assembly property to address the problem of protein denaturation during drug loading process. The HSA rQTY variants described in this study exhibited superior biological activities such as cellular transport, tumor cell-targeting and antitumor efficiency compare to the denatured HSA nanoparticles. More importantly, we now successfully extend the QTY code application to the rQTY code. This simple protein design strategy would provide us with an additional tool for specific hydrophobic modifications of functional proteins with clear-defined binding interfaces, further expand QTY code and rQTY code for protein design with a wide range of applications.

Materials and Methods

Protein Design and Albumin Nanoparticles Preparation. We modified the IB, IIB or IIIB subdomain of natural HSA using a reversed version of previously reported QTY code. Specifically, hydrophilic amino acids (Q/N, T and Y) in α-helices are partially replaced by hydrophobic amino acids (L, V and F) in three subdomains (IB, IIB and IIIB) respectively, based on similarity in electron density maps of amino acid side chains. HSA^{rQTY} solution was injected into PBS solution under sonication. When injection is completed, the ultrasonic dispersion should be stopped to obtain nano-micelles. See *SI Appendix* for full experimental methods and data analysis.

Turbidity Measurements. Turbidity was detected in nephelos turbidity units by the calibrated portable nephelometer. See *SI Appendix* for full experimental methods and data analysis.

Cell Viability. The toxicity of three kinds of HSA^{rQTY} nanoparticles to HEK293T and L929 cells was detected using CCK8 reagent respectively. The co-cultured cells were stained with living-dead cell staining kit and the kit was purchased from BioVision. Inc. See *SI Appendix* for full experimental methods and data analysis.

Experiment of Endocytosis Inhibition. Expression of GP60 and SPARC in two tumor cells (4T1 and A549) and two normal cells (HEK293T and L929) were studied by immunofluorescence. Furthermore, inhibition of endocytosis in tumor cells can be achieved by adding chlorpromazine, amiloride and β-Cyclodextrin simultaneously, and methyl-β-cyclodextrin was added into HUVECs to inhibit the function of GP60 receptor (56). See *SI Appendix* for full experimental methods and data analysis.

Animal Experiments. 1×10^7 4T1-luc cells were injected into subcutaneous right forelimb of each mouse, and tumor-bearing mice were successfully established after 5 d. Then, tumor-bearing mice were administrated according to above groups set. The percent survival curve of tumor-bearing mice in each group was drawn according to recorded data. Nanoparticles labeled with IR783 were injected into the caudal vein of tumor-bearing mice for the tumor-targeting analysis. D-Luciferin potassium working solution was injected into tumor-bearing mice for in vivo observation of tumor size. See *SI Appendix* for full experimental methods and data analysis.

Data, Materials, and Software Availability. All study data are included in the article and/or *SI Appendix*.

ACKNOWLEDGMENTS. This work is supported by the National Natural Science Foundation of China 11972099 and 82202340, Venture & Innovation Support Program for Chongqing Overseas Returnees cx2020079, Scientific and Technological Innovation Project of Chengdu-Chongqing Area Double-city Economic Circle Construction KJCXZD2020007, graduate research and innovation foundation of Chongqing, China CYS21068, and the Fundamental Research Funds for the Central Universities 2021CDJKYJH033.

Author affiliations: [a]Key Laboratory of Biorheological Science and Technology, Ministry of Education, College of Bioengineering, Chongqing University, Chongqing 400030, China; [b]College of Environment and Resources, Chongqing Technology and Business University, Chongqing 400067, China; [c]Department of Pathology, Molecular Medicine and Tumor Center, Chongqing Medical University, Chongqing 400016, China; [d]Department of Neurosurgery, The First Affiliated Hospital of Chongqing Medical University, Chongqing 400042, China; [e]State Key Laboratory of Microbial Metabolism, School of Life Sciences and Biotechnology, Shanghai Jiao Tong University, Shanghai 200240, China; and [f]Media Lab, Massachusetts Institute of Technology, Cambridge, MA 02139

Author contributions: R.M., S.H., R.Q., and S.Z. designed research; R.M. performed research; Y.Y. and H.X. contributed new reagents/analytic tools; R.M., S.H., C.S., Z.H., Y.H., L.W., P.D., J.D., R.Q., and S.Z. analyzed data; J.D. provide resources, funding acquisition; B.W. project administration, Funding acquisition; and R.M., S.H., B.W., R.Q., and S.Z. wrote the paper.

Competing interest statement: S.Z. is a member of board director of 511 Therapeutics that generates therapeutic monoclonal antibodies against solute carrier transporters. He is also a scientific advisor for OH2 Laboratories that works on generating therapeutic monoclonal antibodies against GPCRs. However, this study does not involve in GPCRs and solute carrier transporters. OH2 Laboratories licensed the QTY code technology from Massachusetts Institute of Technology (MIT). However, this article does not study GPCRs. S.Z. is the inventor of the QTY code and has a minor equity of OH2 Laboratories and majority equity in 511 Therapeutics shares that works on solute carrier transporters. S.Z. is also a scientific advisor for 3DMatrix Co Ltd, that commercializes self-assembling peptide hydrogels for surgical and accelerated wound-healing applications. MIT filed several patent applications for the QTY code for GPCRs and glucose transporters. The current study does not involve in GPCRs and glucose transporters. S.Z. is a co-founder and board director of Molecular Frontiers Foundation that encourages young people to ask good questions about science and nature and also organizes Molecular Frontiers Symposia around the world. There is no compensation for the activities.

1. J. W. Myerson *et al.*, Supramolecular arrangement of protein in nanoparticle structures predicts nanoparticle tropism for neutrophils in acute lung inflammation. *Nat. Nanotechnol.* **17**, 86–97 (2022).
2. X. Zeng *et al.*, Blood-triggered generation of platinum nanoparticle functions as an anti-cancer agent. *Nat. Commun.* **11**, 1–12 (2020).
3. A. O. Elzoghby, W. M. Samy, N. A. Elgindy, Albumin-based nanoparticles as potential controlled release drug delivery systems. *J. Control. Release* **157**, 168–182 (2012).
4. E. N. Hoogenboezem, C. L. Duvall, Harnessing albumin as a carrier for cancer therapies. *Adv. Drug Deliv. Rev.* **130**, 73–89 (2018).
5. G. Yang *et al.*, A hypoxia-responsive albumin-based nanosystem for deep tumor penetration and excellent therapeutic efficacy. *Adv. Mater.* **31**, 1901513 (2019).
6. K. Sasaki *et al.*, Engineered collagen-binding serum albumin as a drug conjugate carrier for cancer therapy. *Sci. Adv.* **5**, eaaw6081 (2019).

7. C. E. Callmann *et al.*, Antitumor activity of 1,18-octadecanedioic acid-paclitaxel complexed with human serum albumin. *J. Am. Chem. Soc.* **141**, 11765–11769 (2019).
8. Y. Mizuta *et al.*, A mannosylated, PEGylated albumin as a drug delivery system for the treatment of cancer stroma cells. *Adv. Funct. Mater.* **31**, 2104136 (2021).
9. M. Ikeda-Imafuku *et al.*, Strategies to improve the EPR effect: A mechanistic perspective and clinical translation. *J. Control. Release* **345**, 512–536 (2022).
10. H. Iqbal *et al.*, Serum protein-based nanoparticles for cancer diagnosis and treatment. *J. Control. Release* **329**, 997–1022 (2021).
11. I. de Lázaro, D. J. Mooney, Obstacles and opportunities in a forward vision for cancer nanomedicine. *Nat. Mater.* **20**, 1469–1479 (2021).
12. T. Lin *et al.*, Blood–brain-barrier-penetrating albumin nanoparticles for biomimetic drug delivery via albumin-binding protein pathways for antiglioma therapy. *ACS Nano* **10**, 9999–10012 (2016).
13. S. Gao *et al.*, Albumin tailoring fluorescence and photothermal conversion effect of near-infrared-II fluorophore with aggregation-induced emission characteristics. *Nat. Commun.* **10**, 1–15 (2019).
14. J. V. Gregory *et al.*, Systemic brain tumor delivery of synthetic protein nanoparticles for glioblastoma therapy. *Nat. Commun.* **11**, 1–15 (2020).
15. X. Huang *et al.*, The landscape of mRNA nanomedicine. *Nat. Med.* **28**, 2273–2287 (2022).
16. S. Chen *et al.*, Eradication of tumor growth by delivering novel photothermal selenium-coated tellurium nanoheterojunctions. *Sci. Adv.* **6**, eaay6825 (2020).
17. R. M. Williams *et al.*, Harnessing nanotechnology to expand the toolbox of chemical biology. *Nat. Chem. Biol.* **17**, 129–137 (2021).
18. M. Hama *et al.*, Evidence for delivery of abraxane via a denatured-albumin transport system. *ACS Appl. Mater. Interfaces* **13**, 19736–19744 (2021).
19. Y. Zhao *et al.*, An organic solvent-free technology for the fabrication of albumin-based paclitaxel nanoparticles for effective cancer therapy. *Colloids Surf. B Biointerfaces* **183**, 110394 (2019).
20. S. Sun, T. Chang, G. Lam, Organic solvents-induced difference spectra of bovine serum albumin. *Can. J. Chem.* **61**, 356–361 (1983).
21. Y. Cao, Adipocyte and lipid metabolism in cancer drug resistance. *J. Clin. Invest.* **129**, 3006–3017 (2019).
22. T. Khodaei, S. Inamdar, A. Suresh, A. P. Acharya, Drug delivery for metabolism targeted cancer immunotherapy. *Adv. Drug Deliv. Rev.* **184**, 114242 (2022).
23. D. M. Molina *et al.*, Monitoring drug target engagement in cells and tissues using the cellular thermal shift assay. *Science* **341**, 84–87 (2013).
24. H. Iwamoto, Cancer lipid metabolism confers antiangiogenic drug resistance. *Cell Metab.* **28**, 104–117.e5 (2018).
25. T. Yin *et al.*, A toxic organic solvent-free technology for the preparation of PEGylated paclitaxel nanosuspension based on human serum albumin for effective cancer therapy. *Int. J. Nanomed.* **10**, 7397 (2015).
26. Y. Zhang, D. Zhang, J.-T. Wang, X. Zhang, Y. Yang, Fabrication of stimuli-responsive nanogels for protein encapsulation and traceless release without introducing organic solvents, surfactants, or small-molecule cross-linkers. *Polym. Chem.* **12**, 554–563 (2021).
27. B. Demirkurt, Y. Akdogan, Development of an ionic liquid based method for the preparation of albumin nanoparticles. *ChemistrySelect* **3**, 9940–9945 (2018).
28. D. Cen *et al.*, ZnS@ BSA nanoclusters potentiate efficacy of cancer immunotherapy. *Adv. Mater.* **33**, 2104037 (2021).
29. A. Bunschoten *et al.*, Targeted non-covalent self-assembled nanoparticles based on human serum albumin. *Biomaterials* **33**, 867–875 (2012).
30. R. Wang *et al.*, A nanostructured phthalocyanine/albumin supramolecular assembly for fluorescence turn-on imaging and photodynamic immunotherapy. *ACS Nano* **16**, 3045–3058 (2022).
31. S. Zhang *et al.*, QTY code enables design of detergent-free chemokine receptors that retain ligand-binding activities. *Proc. Natl. Acad. Sci. U.S.A.* **115**, E8652–E8659 (2018).
32. R. Qing *et al.*, QTY code designed thermostable and water-soluble chimeric chemokine receptors with tunable ligand affinity. *Proc. Natl. Acad. Sci. U.S.A.* **116**, 25668–25676 (2019).
33. S. Sugio, A. Kashima, S. Mochizuki, M. Noda, K. Kobayashi, Crystal structure of human serum albumin at 2.5 Å resolution. *Protein Eng.* **12**, 439–446 (1999).
34. M. Bernardi *et al.*, Albumin in decompensated cirrhosis: New concepts and perspectives. *Gut* **69**, 1127–1138 (2020).
35. J. Ghuman *et al.*, Structural basis of the drug-binding specificity of human serum albumin. *J. Mol. Biol.* **353**, 38–52 (2005).
36. J. Jumper *et al.*, Highly accurate protein structure prediction with AlphaFold. *Nature* **596**, 583–589 (2021).
37. Y. Zhang, J. Skolnick, Scoring function for automated assessment of protein structure template quality. *Proteins* **57**, 702–710 (2004).
38. R. Fang, Y. Wang, B. Liu, H. Qian, S. Yang, Characterisation and structure analysis of taxanes-loaded human serum albumin nanoparticles prepared by self-assembly method. *Micro Nano Lett.* **13**, 1057–1062 (2018).
39. S. M. D'Addio, R. K. Prud'homme, Controlling drug nanoparticle formation by rapid precipitation. *Adv. Drug Deliv. Rev.* **63**, 417–426 (2011).
40. D. R. Perinelli *et al.*, Surfactant self-assembling and critical micelle concentration: One approach fits all? *Langmuir* **36**, 5745–5753 (2020).
41. H. Wu, L. Zhu, V. P. Torchilin, pH-sensitive poly(histidine)-PEG/DSPE-PEG co-polymer micelles for cytosolic drug delivery. *Biomaterials* **34**, 1213–1222 (2013).
42. W. M. Aumiller *et al.*, Stimuli responsive hierarchical assembly of P22 virus-like particles. *Chem. Mater.* **30**, 2262–2273 (2018).
43. J. Gao, J. Zhan, Z. Yang, Enzyme-instructed self-assembly (EISA) and hydrogelation of peptides. *Adv. Mater.* **32**, e1805798 (2020).
44. C. E. LaClair, M. R. Etzel, Turbidity and protein aggregation in whey protein beverages. *J. Food Sci.* **74**, C526–C535 (2009).
45. W. Yang *et al.*, Protein-neutral polysaccharide nano- and micro-biopolymer complexes fabricated by lactoferrin and oat beta-glucan: Structural characteristics and molecular interaction mechanisms. *Food Res. Int.* **132**, 109111 (2020).
46. M. Qiu *et al.*, Novel concept of the smart NIR-light–controlled drug release of black phosphorus nanostructure for cancer therapy. *Proc. Natl. Acad. Sci. U.S.A.* **115**, 501–506 (2018).
47. L. Yang *et al.*, Live macrophage-delivered doxorubicin-loaded liposomes effectively treat triple-negative breast cancer. *ACS Nano* **16**, 9799–9809 (2022).
48. C. Liu *et al.*, An orthogonal protection strategy for synthesizing scaffold-modifiable dendrons and their application in drug delivery. *ACS Cent. Sci.* **8**, 258–267 (2022).
49. S. S. Siddiqui *et al.*, Sialoglycan recognition is a common connection linking acidosis, zinc, and HMGB1 in sepsis. *Proc. Natl. Acad. Sci. U.S.A.* **118**, e2018090118 (2021).
50. S. Komatsu, M. Tago, Y. Ando, T. A. Asoh, A. Kikuchi, Facile preparation of multi-stimuli-responsive degradable hydrogels for protein loading and release. *J. Control. Release* **331**, 1–6 (2021).
51. H. J. Li *et al.*, Smart superstructures with ultrahigh pH-sensitivity for targeting acidic tumor microenvironment: Instantaneous size switching and improved tumor penetration. *ACS Nano* **10**, 6753–6761 (2016).
52. E. S. Lee, Z. Gao, Y. H. Bae, Recent progress in tumor pH targeting nanotechnology. *J. Control. Release* **132**, 164–170 (2008).
53. Q. Liu *et al.*, Prodrug-loaded zirconium carbide nanosheets as a novel biophotonic nanoplatform for effective treatment of cancer. *Adv. Sci.* **7**, 2001191 (2020).
54. R. R. Pillai, P. Sreelekshmi, A. Meera, S. Thomas, Biosynthesized iron oxide nanoparticles: Cytotoxic evaluation against human colorectal cancer cell lines. *Mater. Today Proc.* **50**, 187–195 (2022).
55. M. R. Maurya *et al.*, Longitudinal shear stress response in human endothelial cells to atheroprone and atheroprotective conditions. *Proc. Natl. Acad. Sci. U.S.A.* **118**, e2023236118 (2021).
56. N. Desai *et al.*, Increased antitumor activity, intratumor paclitaxel concentrations, and endothelial cell transport of cremophor-free, albumin-bound paclitaxel, ABI-007, compared with cremophor-based paclitaxel. *Clin. Cancer Res.* **12**, 1317–1324 (2006).
57. J. Huang *et al.*, Mechanism of cellular uptake of graphene oxide studied by surface-enhanced Raman spectroscopy. *Small* **8**, 2577–2584 (2012).
58. C. C. Parker, S. E. Lapi, Positron emission tomography imaging of macrophages in cancer. *Cancers* **13**, 1921 (2021).
59. M. M. Leitao, D. de Melo-Diogo, C. G. Alves, R. Lima-Sousa, I. J. Correia, Prototypic heptamethine cyanine incorporating nanomaterials for cancer phototheragnostic. *Adv. Healthc. Mater.* **9**, e1901665 (2020).
60. S. Hao, D. Jin, S. Zhang, R. Qing, QTY code-designed water-soluble Fc-fusion cytokine receptors bind to their respective ligands. *QRB Discov.* **1**, e4 (2020).
61. E. Smorodina *et al.*, Comparing 2 crystal structures and 12 AlphaFold2-predicted human membrane glucose transporters and their water-soluble glutamine, threonine and tyrosine variants. *QRB Discov.* **3**, e5 (2022).
62. E. Smorodina *et al.*, Structural informatic study of determined and AlphaFold2 predicted molecular structures of 13 human solute carrier transporters and their water-soluble QTY variants. *Sci. Rep.* **12**, 20103 (2022).
63. S. Zhang, M. Egli, Hiding in plain sight: Three chemically distinct α-helix types. *Q. Rev. Biophys.* **55**, e7 (2022).
64. K. M. K. Sand *et al.*, Unraveling the interaction between FcRn and albumin: Opportunities for design of albumin-based therapeutics. *Front. Immunol.* **5**, 682 (2015).
65. D. Knauer *et al.*, Albumin-binding and angiogenic domains of SPARC located at its C-terminus. *Cancer Res.* **69**, 2144 (2009).
66. J. T. Andersen *et al.*, Structure-based mutagenesis reveals the albumin-binding site of the neonatal Fc receptor. *Nat. Commun.* **3**, 610 (2012).